

# In Situ Transmission Electron Microscopy Analysis of Copper–Germanium Nanowire Solid-State Reaction

Khalil El hajraoui,<sup>†,‡</sup> Eric Robin,<sup>†,§</sup> Clemens Zeiner,<sup>||</sup> Alois Lugstein,<sup>||</sup> Stéphanie Kodjikian,<sup>†,‡</sup> Jean-Luc Rouvière,<sup>†,§</sup> and Martien Den Hertog<sup>\*,†,‡,||</sup>

<sup>†</sup>Université Grenoble Alpes, F-38000 Grenoble, France

<sup>‡</sup>CNRS, Institut NEEL, F-38000 Grenoble, France

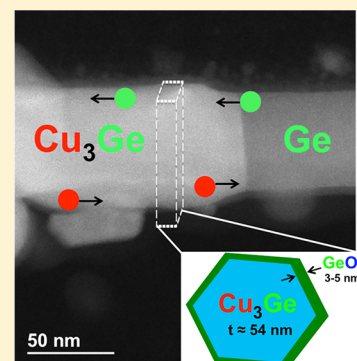
<sup>§</sup>CEA, INAC, F-38000 Grenoble, France

<sup>||</sup>Institute of Solid State Electronics, TU-Wien - Nanocenter Campus Gußhaus, Gußhausstraße 25-25a, Gebäude-CH, A-1040 Wien, Austria

## Supporting Information

**ABSTRACT:** A promising approach of making high quality contacts on semiconductors is a silicidation (for silicon) or germanidation (for germanium) annealing process, where the metal enters the semiconductor and creates a low resistance intermetallic phase. In a nanowire, this process allows one to fabricate axial heterostructures with dimensions depending only on the control and understanding of the thermally induced solid-state reaction. In this work, we present the first observation of both germanium and copper diffusion in opposite directions during the solid-state reaction of Cu contacts on Ge nanowires using in situ Joule heating in a transmission electron microscope. The in situ observations allow us to follow the reaction in real time with nanometer spatial resolution. We follow the advancement of the reaction interface over time, which gives precious information on the kinetics of this reaction. We combine the kinetic study with ex situ characterization using model-based energy dispersive X-ray spectroscopy (EDX) indicating that both Ge and Cu diffuse at the surface of the created  $\text{Cu}_3\text{Ge}$  segment and the reaction rate is limited by Ge surface diffusion at temperatures between 360 and 600 °C. During the reaction, germanide crystals typically protrude from the reacted NW part. However, their formation can be avoided using a shell around the initial Ge NW.  $H_a$  direct Joule heating experiments show slower reaction speeds indicating that the reaction can be initiated at lower temperatures. Moreover, they allow combining electrical measurements and heating in a single contacting scheme, rendering the Cu–Ge NW system promising for applications where very abrupt contacts and a perfectly controlled size of the semiconducting region is required. Clearly, in situ TEM is a powerful technique to better understand the reaction kinetics and mechanism of metal–semiconductor phase formation.

**KEYWORDS:** Ge nanowires, solid-state reaction, in situ transmission electron microscopy, energy dispersive X-ray spectroscopy, surface diffusion



Nowadays semiconductor nanowires (NWs) are very promising candidates in many research fields ranging from electronics<sup>1,2</sup> and optoelectronics<sup>3</sup> to energy conversion<sup>4</sup> and spintronics.<sup>5</sup> Many different device developments start to emerge thanks to the bottom up fabrication approach of semiconductor materials, capable of growing high quality heterostructures providing good electrical and optical performance in NWs.

Most electrical contacts between metal and Ge NWs are realized using a conventional electron beam lithography process, metal deposition, and lift-off techniques. Therefore, the dimensions that can be obtained depend on the resolution of the lithography process. For some combinations of metal–semiconductor NW contacts, an annealing step can initiate a solid-state reaction where a metal enters the NW extremities and creates an intermetallic region.<sup>6–10</sup> Typically, very abrupt interfaces can be obtained between the metallic phase and the

remaining segment length of the semiconducting NW,<sup>8–12</sup> with dimensions of this segment that no longer depend on the resolution of the lithography technique but on the control of the solid-state reaction. This heterostructure phase formation is referred to as silicidation in Si and germanidation in Ge bulk structures or NWs.

Many studies used this process to achieve high performance devices using different metals (Ni,<sup>6,7</sup> Cu,<sup>9,13</sup> Al,<sup>11</sup> and Mn<sup>14,10</sup>) in the Ge NW system to form a low resistivity germanide with the aim to increase NW device performance. With respect to other silicides, the  $\text{Cu}_3\text{Ge}$  is particularly interesting due to its low resistivity and the high current density it can sustain<sup>9,15,16</sup> The solid-state reaction in all these previous works<sup>6,7,9,10,13,14</sup>

**Received:** May 2, 2019

**Revised:** September 30, 2019

**Published:** October 15, 2019

was activated by a conventional thermal heating process either ex situ using a rapid thermal annealing (RTA) or in situ in a transmission electron microscope (TEM) using a heating stage.<sup>17,18</sup> In the following, we will report an in situ TEM study comparing this more conventional heating treatment while monitoring the sample temperature (i.e., heating the entire contacted NW) and uncalibrated annealing experiments where a local Joule heating is used, referred to as direct Joule heating. In this last case, a current flowing through the metal also used to contact the NW starts the reaction, as demonstrated in Mongillo et al.,<sup>19</sup> allowing a solid-state reaction to occur at the contact point between the metal and the Ge NW. We perform all these experiments in situ in TEM to follow all the phenomena that occur during the metal–germanium phase formation with nanometer spatial resolution in real time with the aim to better understand reaction kinetics and the mechanism of metal/semiconductor phase formation in the Cu/Ge NW system.

**Experimental Methods.** The NWs used in these experiments were undoped gold-catalyzed Ge NWs, synthesized via the vapor liquid solid (VLS) process along the  $\langle 111 \rangle$  growth direction with diameters ranging from 10 to 80 nm. Growth parameters are described elsewhere.<sup>9</sup> Ge NWs were dispersed in ethanol using ultrasonic vibrations. The Ge NW solution was drop casted on three different silicon nitride ( $\text{Si}_3\text{N}_4$ ) membranes: a commercial heater chip calibrated in temperature from DENSsolutions,<sup>20</sup> homemade membranes with a 50 nm thick ( $\text{Si}_3\text{N}_4$ ) layer on a 300  $\mu\text{m}$  Si frame, and a commercial  $\text{Si}_3\text{N}_4$  holey membrane. The membrane fabrication process is described by den Hertog et al.<sup>21</sup> For direct Joule heating experiments, two parallel strip lines are defined on each end of a Ge NW using e-beam lithography and then dipped in a diluted hydroiodic acid  $[\text{HI}/\text{H}_2\text{O}][1:7]$  for 5 s and rinsed with DI water to remove the native oxide from the Ge NW surface at the contact region before Cu deposition (110 nm) using e-beam evaporation. These four Cu contacts are connected to large Ti (10 nm)/Au (50 nm) pads defined prior to NW dispersion by laser lithography to ensure a good electrical connection between the sample and the TEM sample holder, see Figure 1a,c. The contacted NW can be locally heated by flowing a current through one of the strip lines creating a Joule heating current  $I_{\text{heating}}$ , see Figure 1b. For direct Joule heating experiments an asymmetrical positive  $V^+$  and negative  $V^-$  voltage was applied on both ends of a Cu metal line to decouple the heating current from a potential current through the NW,  $I_{\text{NW}}$ , that can be measured with an amperemeter providing a real time measurement of the current during the germanide process, see Figure 1b. Furthermore, we used commercial membranes calibrated in temperature, where a buried heating spiral in a SiN membrane is heated by Joule heating. We dispersed Ge NWs on 20 nm thick  $\text{Si}_3\text{N}_4$  windows in such a membrane (see Supporting Information (SI) Figure S1). These NWs were contacted on one side with a Cu strip line providing the Cu reservoir, using the same lithography process as defined above. All the heating experiments were carried out in situ in a TEM Philips CM300 working at 100 kV equipped with a CMOS camera from TVIPS or in an FEI Titan at 80 kV using a DENSsolutions double-tilt six-contact biasing sample holder (see Figure 1c). An acceleration voltage below 150 kV was used to avoid knock-on damage, creation of vacancies, and related modifications of electrical and diffusion properties. Structural characterization of different samples was performed posterior

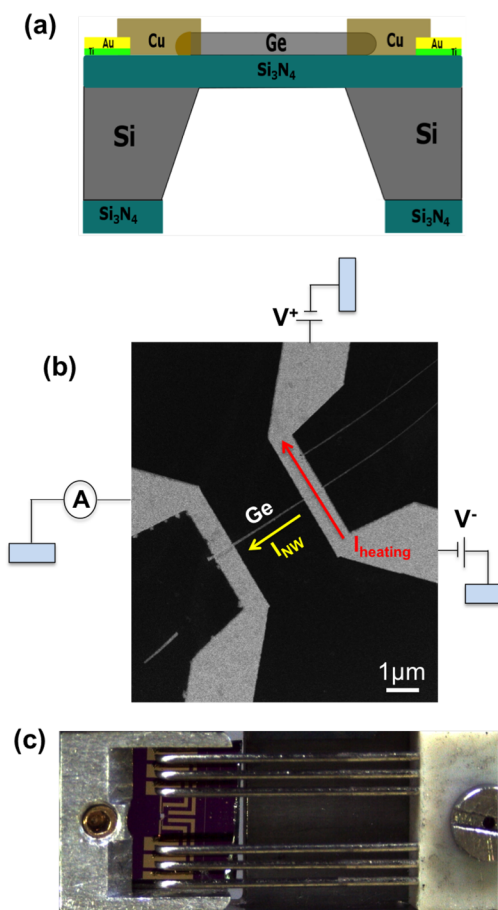


**Figure 1.** Illustration of the Joule heating technique  $H_a$  allowing the germanide formation. (a) Schematic of a cross-sectional view representing a contacted Ge NW on a silicon nitride membrane. The Ge NW is contacted by Cu metal pads which are connected to the sample holder via Ti/Au pads contacted by small needles. (b) HAADF-STEM image showing a top view of a connected Ge NW by two Cu metal strip lines. Cu contacts are heated one at a time via a heating current  $I_{\text{heating}}$  driven by the voltage difference ( $V^+ - V^-$ ) while measuring the current  $I_{\text{NW}}$  through the Ge NW. (c) Photograph of microfabricated membrane loaded on a six-contact biasing sample holder from DENSsolution.

to the heating experiments or ex situ using the same microscopes. Chemical characterization was carried out ex situ in a state of the art FEI Osiris or Titan Themis (at 200 kV), equipped with four Silicon Drift Detectors using an ultranarrow gap Fischione tomography sample holder, which allows a large solid angle for signal detection.

**Results.** In Figure 2, several heating experiments are compared: heating using direct Joule heating in a metal strip on the Ge NW, that we will call  $H_a$  (Figure 2a) and a membrane–substrate Joule heating using a DENSsolution heater chip,  $H_b$  (Figure 2b,c) at two temperatures, 410 and 600  $^\circ\text{C}$ . Movies of the germanide propagation experiments using both heating techniques are shown in the SI (Movie S1, Movie S2, and Movie S3). The contrast change in the Ge NW present in the TEM bright-field (BF) images indicates the metal intrusion in the NWs. To investigate the kinetics of the germanide phase formation, we followed the progression of the germanide interface as a function of time, where  $L$  is the distance the reaction interface has traveled. Three different examples of these traces are shown in Figure 2d–f, where both

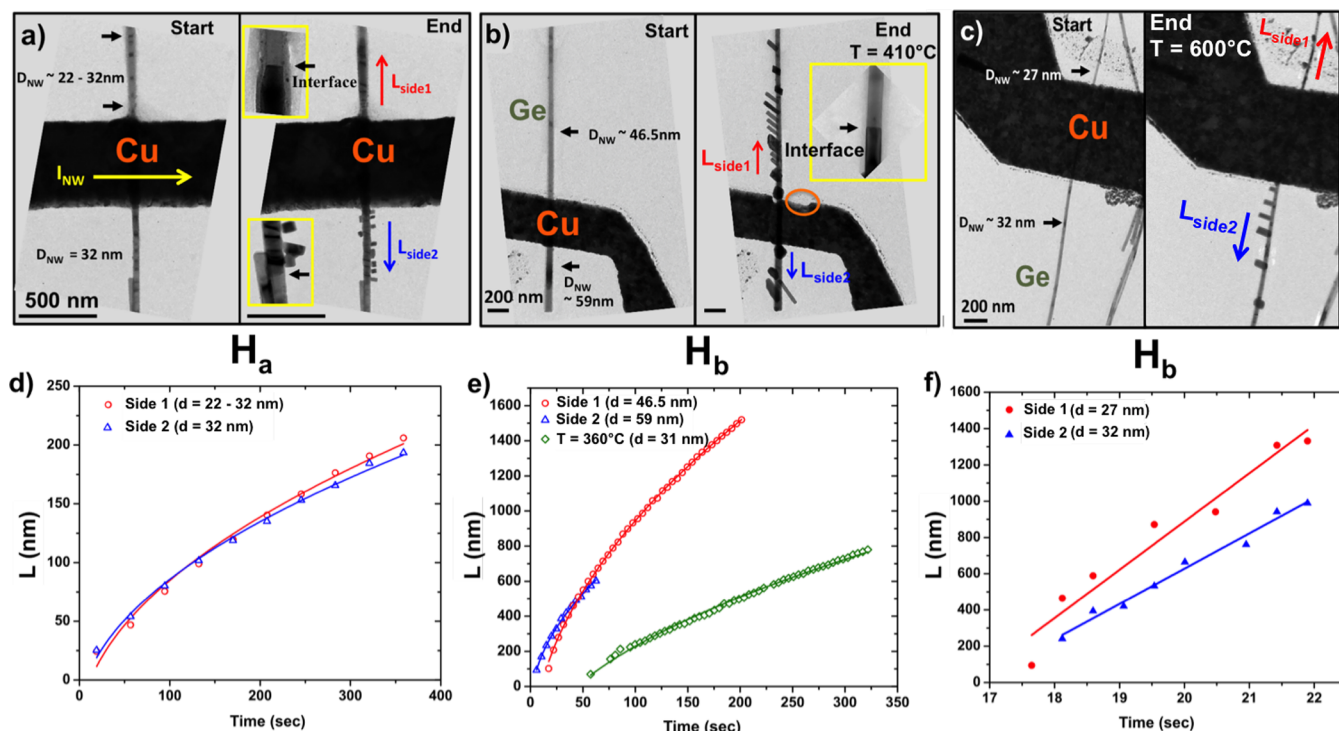


**Figure 2.** In situ copper–germanium phase propagation experiments using both in situ Joule heating ( $H_a$ ) and membrane–substrate Joule annealing ( $H_b$ ). (a) TEM image showing the sample heated using in situ  $H_a$ , both sides have a similar NW diameter ( $d_{NW} = 32$  nm). (b,c) TEM images of in situ heating experiments  $H_b$  at two different temperatures 410 and 600 °C, respectively. The two sides of the NWs have different NW diameters. (d) The length of germanide segment versus time at  $\Delta V = 0.75V$  using in situ  $H_a$  for both opposite propagation directions  $L_{side1}$  (red open circle; fit, red line) and  $L_{side2}$  (blue open triangle; fit, blue line). (e,f) The length of the germanide segment versus time at three different temperatures: 360 °C (green open diamond; fit, green line) (TEM image not shown), 410 °C (red open circle, blue open triangle) and fit (red line, blue line), and 600 °C (red-closed circle, blue-closed diamond) and fit (red line, blue line). Profiles in panel d and e can be well fitted with a square root function (see eq 1). Profiles in panel f fit well with a linear function. All the samples reveal an influence of the NW diameter on the reaction speed.

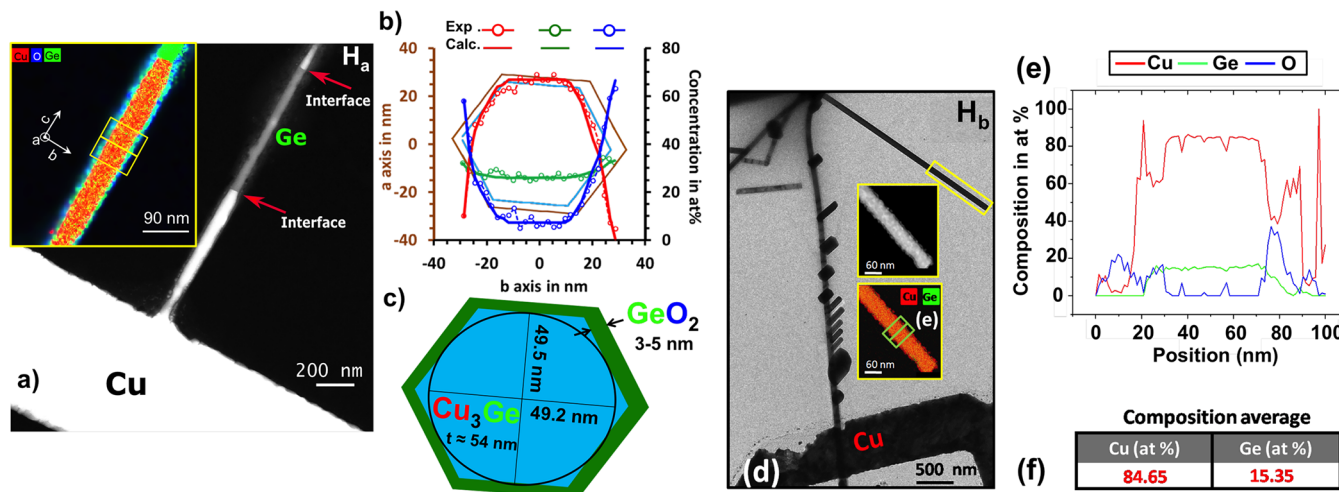


**Figure 3.** (S)TEM images and EDX quantification (line scan and hypermap) of different elements (blue = O, red = Cu, green = Ge) in the NW after  $H_a$  ( $V_{heat} = 0.775$  V) and  $H_b$  ( $T = 600$  °C) experiments. (a) HAADF STEM image of a copper–germanium sample heated using  $H_a$ . The inset shows an EDX hypermap of the  $Cu_3Ge$  region. (b) Cu (red ○), Ge (green ○), and O (blue ○) average concentration (atom %) and local thickness profiles along the line shown in the inset in panel a. (c) Schematic of the NW cross-section composed of different core–shell layers after heating. The hexagon used to fit the experimental EDX data is constructed using the tangents to an ellipse (see SI of ref 24) that is indicated in the schematic together with its dimensions. (d) TEM image of a heated sample at ( $T = 600$  °C) using  $H_b$ . Inset images show an STEM and an EDX hypermap of the crystal formed after heating at  $T = 600$  °C (e) Line scan of Cu (red), Ge (green), and O (blue) concentration in atom % along the region defined in the inset image in panel d. (f) A local concentration in atom % of both Cu and Ge on the crystal core.

$H_a$  and  $H_b$  heating techniques were used. TEM images of a copper–Ge NW system before and after germanide phase

formation heated using  $H_a$  at ( $V_{heat} = 0.75$ – $0.775$  V) are shown in Figure 2a. The particularity of this sample is an

unintentional shell around the Ge NW above the contact ( $L_{\text{side1}}$ ) that is probably due to the remaining resist from the lithography process. During the heating experiment, we noticed the absence of any protruding crystals in  $L_{\text{side1}}$  in contrast to  $L_{\text{side2}}$  and all other studied samples. Yet, the interface evolution appears not influenced by the protruding crystals comparing the length of the germanide segment formed in the NW sides with and without crystals ( $L_{\text{side1}} \simeq L_{\text{side2}}$ ) during the phase propagation, see Figure 2d. In Figure 2b,c, TEM images of a heated sample at 410 and 600 °C using  $H_b$  are shown, respectively. All samples heated using  $H_a$  or  $H_b$  at low temperature (360–410 °C) evidence a parabolic growth behavior and were well fitted using a square root function of the form.<sup>22,23</sup>

$$L = \sqrt{2Dt} \quad (1)$$

where  $L$  is the germanide length in nanometers,  $D$  is the diffusion constant ( $\text{nm}^2/\text{s}$ ), and  $t$  is time in seconds. On the other hand, at 600 °C the front progresses linearly as a function of time. Moreover, an incubation time was observed in the sample heated using  $H_b$  at 410 °C (see Movie S2), where the propagation started later in the NW on the right. The germanide growth rate varies depending on the Ge NW diameter in all heated samples. The smaller diameter NW (plotted in red, Figure 2) always showed a faster propagation of the reaction front. After heating at 410 °C to obtain the images in Figure 2b, we observed that the reaction had not started in every contacted NW on the sample (only 4 out of 42 contacted NWs were activated and gave rise to the germanide phase formation). Therefore, the second heating was applied with the aim to activate the solid-state reaction in the other contacted NWs present on the sample. To investigate possible reasons for delayed activation of the solid-state reaction in the contacted NWs, we prepared another sample. In complement to the chemical processing (HI/ $\text{H}_2\text{O}$ ), an Ar plasma of 30 s was applied to remove any native oxide left on the NW before metal deposition. Although the solid-state reaction started in more NWs (26 out of 32 contacted NWs) compared to the previous sample and at a lower temperature ( $T = 360$  °C), again the reaction did not start in all contacted NWs. This reveals that the additional Ar plasma provides a better Cu–Ge NW contact, however the contact is still not clean enough to start the reaction in all contacted NWs.

To confirm the chemical composition of the germanide phase formed after  $H_a$  and  $H_b$  heating experiments, an EDX analysis at 200 kV was performed in different samples.

Figure 3a represents an high-angle annular dark-field–scanning transmission electron microscopy (HAADF–STEM) image of the sample shown above in Figure 2a heated using  $H_a$ . The brighter part corresponds to  $\text{Cu}_3\text{Ge}$  and the darker part to Ge, as we will show below. The inset represents an EDX hypermap with a representation of the electron beam direction denoted  $a$  and the respective scan directions denoted  $b$  and  $c$  ( $c$  being the NW axis).

To provide a better quantitative analysis of the hypermap, we use an NW model as presented by Rueda et al.<sup>24</sup> Using the sample thickness extracted from the total X-ray count, a model of an hexagonal cross-section NW including different layers, is calculated and compared with the experimental data to obtain a best fit. A reconstruction of the germanide cross-section extracted from the hypermap is represented in Figure 3b. We find a core–shell cross-section of two imbricated hexagons: a thick  $\text{Cu}_3\text{Ge}$  core  $t \sim 54$  nm, surrounded by a shell of a  $\text{GeO}_2$

oxide  $t \sim 3$ –5 nm. The  $\text{Cu}_3\text{Ge}$  composition is coherent with the results by Burchhart et al.<sup>9</sup>

Figure 3c illustrates the distribution of these different layers forming the NW cross-section. The curves in Figure 3b with symbols (red --O--, green --O--, blue --O--) are the atom concentrations deduced directly from the net experimental X-ray intensities of each element using the zeta factor method<sup>25</sup> and the (red line, green line, blue line) curves are the calculated concentration profiles using the hexagonal model of the NW cross-section. To achieve a complete cross-section model, at least two X-ray maps acquired at two tilt angles are required,<sup>24</sup> however the observation of a core–shell structure remains valid even though only one orientation was used to reconstruct the NW cross-section, which is possible due to the symmetry of the NW section. The NW has a hexagonal cross-section, which was confirmed by the measured thickness profile.

Additionally, after heating at 600 °C (Figure 2c), we performed EDT on a large protruded crystal, see at the start of Section II of the SI and ref 26. Figure 3d shows a TEM image of the NW after the germanide formation process at 600 °C where the same protruded crystal is outlined by the yellow box and the inset images represent an HAADF–STEM image and an EDX hypermap of the selected region, respectively. A concentration profile obtained in the inset of Figure 3d is shown in Figure 3e, showing the quantified concentration in atom % of different elements present, obtained using the Cliff–Lorimer quantification method. The average concentration of Cu and Ge determined along the line scan is shown in Figure 3f. The EDX results confirm the EDT analysis concluding on the  $\text{Cu}_3\text{Ge}$  phase formation at 600 °C.

Furthermore, the EDX analysis was extended to the Cu metal at the side of the NW heated using  $H_a$  ( $V_{\text{heat}} = 1.15$  V). Figure 4 shows an HAADF–STEM image of the Cu metal pad, revealing contrast caused by grain boundaries in the polycrystalline Cu. The inset image is an EDX hypermap at the same location on the Cu contact showing the incorporation of Ge atoms along grain boundaries in the metal. The Ge atom incorporation in Cu grain boundaries was detected on a large area of the Cu metal, revealing an important amount of Ge

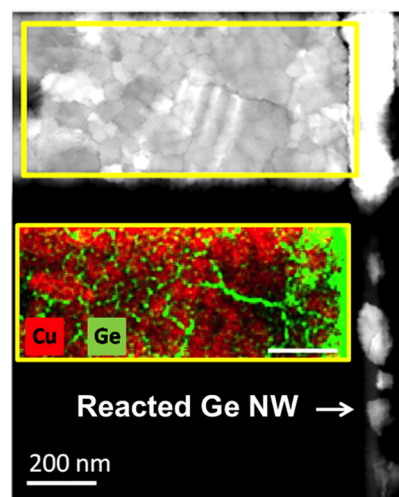


**Figure 4.** STEM image and EDX hypermap of Cu and Ge elements present in the Cu metal next to the NW after phase propagation using  $H_a$  ( $V_{\text{heat}} = 1.15\text{V}$ ). The Ge atoms appear to diffuse in the metal grain boundaries.

**Table 1.** Summary of Different Experiments Performed on Copper–Germanium Samples Using Both  $H_a$  and  $H_b$  Heating Techniques<sup>a</sup>

| Heating | Temperature                         | Diameter   | Curve Behavior | Fit Coefficient   | Remarks                                   |
|---------|-------------------------------------|--|----------------|---|---|
| $H_b$   | 360 °C                              | $D_{\text{side1}} = 31 - 25 \text{ nm}$ ; $D_{\text{side2}} = 37 \text{ nm}$ | Square root    | $P_{\text{side1}} = 62.3$ ; $P_{\text{side2}} = \text{can't be fit}$                | Size dependence                           |
| $H_b$   | 410 °C                              | $D_{\text{side1}} = 46.5 \text{ nm}$ ; $D_{\text{side2}} = 59 \text{ nm}$    | Square root    | $P_{\text{side1}} = 137.5$ ; $P_{\text{side2}} = 93.3$                              | Size dependence                           |
| $H_b$   | 600 °C                              | $D_{\text{side1}} = 25.5 \text{ nm}$ ; $D_{\text{side2}} = 32 \text{ nm}$    | Linear         | $P_{\text{side1}} = 246.94 \text{ nm/s}$ ; $P_{\text{side2}} = 194.46 \text{ nm/s}$ | Size dependence                           |
| $H_a$   | $V_{\text{heat}} = 0.625 \text{ V}$ | $D_{\text{side1}} = 72 - 62 \text{ nm}$                                      | Square root    | $P_{\text{side1}} = 44.4$   | —   |
| $H_a$   | $V_{\text{heat}} = 1.15 \text{ V}$  | $D_{\text{side1}} = 50 \text{ nm}$   | Square root    | $P_{\text{side1}} = 22.4$   | —   |
| $H_a$   | $V_{\text{heat}} = 0.775 \text{ V}$ | $D_{\text{side1}} = 31 \text{ nm}$ ; $D_{\text{side2}} = 32 \text{ nm}$      | Square root    | $P_{\text{side1}} = 14.7$ ; $P_{\text{side2}} = 15.12$                              | Crystals show no influence in propagation |

<sup>a</sup>All samples show a square root evolution of the reaction interface location as a function of time, except at high temperature where the evolution is linear. A size dependence is clearly visible in the fit-coefficient of the length-curves reported for different diameter NWs heated with both techniques. Curves showing a square root were fit with an equation similar to eq 1:  $P\sqrt{t}$  and linear curves were fit with  $Pt$ . The slope  $P$  is equal to the constants  $A$  or  $B$  (defined as  $A = 4D \frac{\delta}{R} (\frac{1}{k_1} + \frac{R}{D_3})$  and  $B = 4D \frac{\delta}{R} \frac{C_{\text{res}}}{N}$  of the diffusion model described in SI Section VI).

atoms exchanged between the NW and the metal during the germanide phase formation. Similar results were found for  $H_b$  heating experiments. This result reveals that both species are moving during germanide phase formation.

**Discussion.** In the following, we will combine both kinetic and structural analysis results to provide a better understanding of the germanide growth rate in a Ge NW. Table 1 represents a summary of all performed experiments.

We notice a square root behavior of the reaction interface as a function of time in all heated samples following eq 1, except for the  $H_b$  experiment at 600 °C, where the germanide front progresses linearly as a function of time. The germanide growth rate at low temperature appears therefore to be limited by a diffusion process. As observed in Figure 2d,e the propagation rate is systematically faster in smaller diameter NWs.

According to the model presented by Tang et al.<sup>27</sup> an influence of the radius indicates a reaction limited by surface diffusion, which is coherent with a high-resolution STEM image of the interface where the  $\text{Cu}_3\text{Ge}$  appears to protrude further into the NW at the surface (see Figure S2).

Several papers have presented kinetic studies of metal phases in semiconducting NWs,<sup>27–31</sup> mostly on the NiSi system. In these studies, surface diffusion was reported to be the rate limiting step of the metal phase propagation. In all these previous studies, metal atoms have been reported as the only or the dominant diffusing species during the silicide phase formation. The kinetic studies clearly indicate that the reaction rate is limited by a surface diffusion process, whereas the EDX results demonstrate that both metal as well as semiconductor atoms are moving in opposite directions, as illustrated in Figure 5.

For the diffusion of Al in Ge NWs, it has been shown that a thin Ge layer is present at the surface of the created Al segment,<sup>32</sup> attributed to surface diffusion of Ge on the created Al segment. In the Cu–Ge (NW) system we cannot clearly demonstrate the presence of either Ge or Cu thin surface layers because they are present on a  $\text{Cu}_3\text{Ge}$  core, complicating the analysis with respect to the presence of a Ge layer on a pure Al section. Indeed, taking into account very thin Ge and Cu layers at the surface of the created  $\text{Cu}_3\text{Ge}$  segment in the modeling of the NW does improve the quality of the fit to the experimental data, (as shown in SI Figure S3). However, the improvement of the fit is not sufficient to clearly demonstrate the presence or

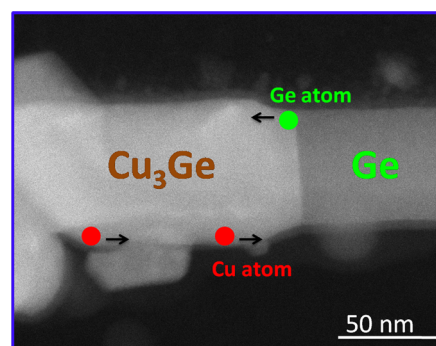


**Figure 5.** STEM image with schematic illustrating the diffusion processes that occur during the germanide formation. Both Cu and Ge atoms diffuse close to the surface. Cu diffuses to the reaction interface and Ge diffuses to Cu metal grain boundaries in the Cu reservoir.

absence of such very thin surface layers. It should also be noted that the fit improves only for adding both thin Cu and Ge layers (compare SI Figure S3a,d).

Indeed, if Cu was the only diffusing species, a large NW diameter change would be expected during the reaction as three times as many Cu atoms as originally present Ge atoms incorporate in the NW. However, hardly any diameter change is observed, see Figure 2a,b.

The question that can be addressed now is which of these two elements limits the reaction speed? To answer this question two additional observations need to be considered: (i) we followed the growth of a protruding crystal, see SI Figure S4, and find that the length of the crystal over time follows eq 1, indicating a diffusion process as a rate limiting step for growth of these crystals. (ii) We could also observe what happens when the propagation front moves into a crossing NW, which was observed in the  $H_b$  experiment at 410 °C, see Movie S2. In SI Figure S5 we see that the propagation in the original NW slows down when the propagation starts in the crossing NW.

From a basic calculation presented in Supporting Information Section III, we find that twice as much Cu atoms enter the NW to form the  $\text{Cu}_3\text{Ge}$  phase than Ge atoms that diffuse out into the Cu contact. This simple analysis shows that Cu is the dominant diffusing species, however, it does not tell us which species limits the reaction speed. The protruding crystals have

Table 2. Diffusion Coefficients of Cu and Ge Systems at 500 °C

|   | copper in germanium     | copper in Cu <sub>3</sub> Ge | germanium in germanium   | copper in copper        |
|---|-------------------------|------------------------------|--------------------------|-------------------------|
| $D$ (cm <sup>2</sup> ·sec <sup>-1</sup> ) | $3.06 \times 10^{-633}$ | $10^{-10}$ – $10^{-834}$     | $9.34 \times 10^{-2035}$ | $3.04 \times 10^{-436}$ |

the same composition and are in epitaxy with the transformed region of the NW (see Figure S6) and therefore contain mostly Cu. Indeed, if the reaction would be limited by the supply of Cu from the reservoir, we expect an influence of propagation speed when protruding crystals are formed, as they will consume a considerable amount of Cu from the supply. However, as we have observed in Figure 2a,d, the propagation rate is not influenced by the crystals growing out of the transformed NW and the diameter of the nanowire did hardly change. On the other hand, the propagation rate is decreased when the reaction front continues into a crossing NW, see Movie S2 and Figure S5. These observations could indicate that the reaction rate is limited by surface diffusion of Ge. In this case, the reaction speed will not be influenced by the protruding crystal growth, as the Ge diffusing from the reaction interface toward the Cu reservoir still needs to diffuse in a surface channel over a part of the transformed NW region (and then goes either into the protruding crystal or into the Cu reservoir) and it explains why the reaction is slowed down for propagation in a crossing NW as it doubles the amount of Ge that needs to be evacuated through the surface channel on the original NW into the Cu reservoir.

Therefore our results indicate that Ge surface diffusion on the Cu<sub>3</sub>Ge segment is the rate limiting step. The question now is why Ge atoms prefer to diffuse on the germanide surface instead of diffusing in the Ge NW (giving rise to a Ge self-diffusion), the answer is presented in Table 2: the Ge self-diffusion coefficient is very low. Therefore, the diffusion of Ge atoms on the surface of the Cu<sub>3</sub>Ge segment is energetically favorable.

The diffusion model described in SI Section IV based on previous publications<sup>27,29–31</sup> presents the three potential rate limiting steps and is constructed assuming that Ge atom movement is the rate limiting step. The different regimes governing the propagation are summarized in Table 3.

Table 3. Summary of the Different Regimes Governing the Germanide Phase Propagation Deduced from Equation S12

| germanide growth regimes                                       | $L$                                   |
|--|---------------------------------------|
| Ge NW - germanide interface limited ( $t \ll \frac{A^2}{2B}$ ) | $\sim t$ (independent of $R$ )        |
| germanide - Cu interface limited ( $t \ll \frac{A^2}{2B}$ )    | $\sim R^{-1}t$                        |
| volume diffusion limited ( $t \gg \frac{A^2}{2B}$ )            | $\sim \sqrt{t}$ (independent of $R$ ) |
| surface diffusion limited ( $t \gg \frac{A^2}{2B}$ )           | $\sim \left(\frac{t}{R}\right)$       |

From this model we find the surface diffusion equation resulting from eq S12

$$L = \sqrt{Bt} = \sqrt{\frac{C_{\text{res}}}{N} \frac{\delta}{R} 4D^s t} \quad (2)$$

where  $\delta$  is the thickness of the near surface-diffusion layer. We used a value of 0.8 nm for the diffusion layer thickness, which may be in accordance with the EDX data, see SI Figure S3. We applied this equation on the data shown in Table 1 to obtain the surface-diffusion coefficient of Ge on the Cu<sub>3</sub>Ge NW

segment, which is summarized at different temperatures in Table 4. At 600 °C, a linear relation between  $L$  and  $t$  has been

Table 4. Calculated Surface-Diffusion Coefficients Using the Fitted Values from Table 1 by Equation 2 for  $D^s_{\text{Ge}}$ 

|       | heating      | $D^s_{\text{Ge}}$ (cm <sup>2</sup> /sec) surface diffusion |
|-------|--------------|--|
| $H_b$ | $T = 360$ °C | $2.55 \times 10^{-9}$                                      |
|       | $T = 410$ °C | $1.47 \times 10^{-8}$                                      |

observed influenced by the NW diameter. According to Tang et al.<sup>27</sup> (see also SI Section IV) this can indicate a reaction limited by the metal–NW interface or the germanide–Ge NW interface. However, in the first case an influence of NW diameter is expected where no diameter influence is expected for the second case. According to Table 3 this can therefore indicate a reaction limited by the metal–NW interface as a diameter influence was observed. Two possible explanations can be proposed for the linear growth rate behavior based on the equations represented in Table 3. Either the diffusion through the metal is very slow compared to the diffusion through the wire itself, or the contact section where the diffusion occurs in the metal is very small with respect to the NW section.

It can be seen from Table 1 that the propagation speed and related diffusion constant are systematically lower in  $H_a$  experiments with respect to  $H_b$ . Therefore, we expect that the temperature is also systematically lower in  $H_a$  experiments that are not temperature calibrated. This speculation was confirmed by finite element simulations (Comsol).<sup>26</sup> Because in  $H_b$  experiments at lower temperatures no reaction was observed, this could indicate that the presence of an electrical current in the metal strip on the NW could facilitate nucleation of the Cu<sub>3</sub>Ge phase.

In summary, this work presents a detailed TEM in situ study of the solid-state reaction using Joule heating  $H_a$  and controlled temperature  $H_b$  heating experiments. Quantitative EDX analysis showed that Ge–Cu<sub>3</sub>Ge heterostructures are formed below 600 °C and a copper rich Cu<sub>5</sub>Ge phase is formed at 600 °C. Kinetic analysis of the germanide segment length as a function of time using both types of heating experiments shows a systematically faster reaction rate in thinner NWs. The rate limiting step appears to be Ge surface diffusion and the Cu/nanowire interface seems to be the critical factor for the germanide reaction initiation.

EDX maps reveal that in the Cu pad, the Ge is mainly incorporated at the Cu grain boundaries and not in the Cu grains, demonstrating that Cu and Ge are diffusing in opposite directions.

$H_a$  direct Joule heating experiments show slower reaction speeds indicating that the reaction can be initiated at lower temperatures. Moreover they allow combining electrical measurements and heating in a single contacting scheme. During the reaction, germanide crystals typically protrude from the reacted NW part. Their formation can however be avoided using a shell around the initial Ge NW, rendering this system promising for applications where very abrupt contacts and a perfectly controlled size of semiconducting region is required.

## ■ ASSOCIATED CONTENT

### Supporting Information

Supporting methods and data. This material is available free of charge via the Internet at <http://pubs.acs.org/>. The Supporting Information is available free of charge on the ACS Publications website at DOI: 10.1021/acs.nanolett.9b01797.

Movie M1: TEM bright field in-situ experiment using Ha, exposure time 0, 5 sec, 7 fps (MP4)

Movie M2: TEM bright field in-situ experiment using Hb at 410 °C, exposure time 0, 5 sec, 7 fps (MP4)

Movie M3: TEM bright field in-situ experiment using Hb at 600 °C, exposure time 0, 5 sec, 7 fps (AVI)

(Figure S1) Description of calibrated heating membranes; (Figure S2) high-resolution HAADF STEM analysis of Ge NW/Cu<sub>3</sub>Ge interface; (Figure S3) 3D reconstruction of the cross-section of the transformed Cu<sub>3</sub>Ge segment; (Figure S4) heating experiment at 410 °C and position of the interface (*L*) as a function of time; (Figure S5) heating experiment at 410 °C and position of the interface (*L*) as a function of time in crossing NWs; (Figure S6) high-resolution HAADF-STEM analysis of Cu<sub>3</sub>Ge protruding crystals; (Figure S7) schematic illustrating the transformed Ge NW after heating experiments; (Figure S8) schematic illustrating the different mechanisms taking place during the germanide growth. (PDF)

## ■ AUTHOR INFORMATION

### Corresponding Author

\*E-mail: [martien.den-hertog@neel.cnrs.fr](mailto:martien.den-hertog@neel.cnrs.fr). Phone: +33 (0)4 76881045.

### ORCID

Khalil El hajraoui: 0000-0002-7627-6981

Alois Lugstein: 0000-0001-5693-4775

Martien Den Hertog: 0000-0003-0781-9249

### Notes

The authors declare no competing financial interest.

## ■ ACKNOWLEDGMENTS

The authors thank T. Fournier and B. Fernandez for their technical support. Financial support from the ANR JCJC COSMOS (ANR-12-JS10-0002), the French CNRS, and CEA is acknowledged. We benefited from the access to the technological platform NanoCarac of CEA-Minatech and Nanofab from institute NEEL, Grenoble. Furthermore, the authors from Grenoble and Vienna received traveling support from the AMADEUS/CampusFrance program.

## ■ REFERENCES

- (1) Tomioka, K.; Yoshimura, M.; Fukui, T. *Nature* **2012**, *488*, 189–192.
- (2) Duan, X.; Huang, Y.; Cui, Y.; Wang, J.; Lieber, C. M. *Nature* **2001**, *409*, 66–69.
- (3) Joyce, H. J.; Gao, Q.; Hoe Tan, H.; Jagadish, C.; Kim, Y.; Zou, J.; Smith, L. M.; Jackson, H. E.; Yarrison-Rice, J. M.; Parkinson, P.; Johnston, M. B. *Prog. Quantum Electron.* **2011**, *35*, 23–75.
- (4) Peng, K.-Q.; Wang, X.; Li, L.; Hu, Y.; Lee, S.-T. *Nano Today* **2013**, *8*, 75–97.
- (5) Hrkac, G.; Dean, J.; Allwood, D. A. *Philos. Trans. R. Soc., A* **2011**, *369*, 3214–3228.

(6) Tang, J.; Wang, C.-Y.; Xiu, F.; Lang, M.; Chu, L.-W.; Tsai, C.-J.; Chueh, Y.-L.; Chen, L.-J.; Wang, K. L. *ACS Nano* **2011**, *5*, 6008–6015.

(7) Dellas, N. S.; Minassian, S.; Redwing, J. M.; Mohny, S. E. *Appl. Phys. Lett.* **2010**, *97*, 263116.

(8) Hsu, S.-C.; Hsin, C.-L.; Huang, C.-W.; Yu, S.-Y.; Wang, C.-W.; Lu, C.-M.; Lu, K.-C.; Wu, W.-W. *CrystEngComm* **2012**, *14*, 4570–4574.

(9) Burchhart, T.; Lugstein, A.; Hyun, Y. J.; Hochleitner, G.; Bertagnolli, E. *Nano Lett.* **2009**, *9*, 3739–3742.

(10) Tang, J.; Wang, C.-Y.; Hung, M.-H.; Jiang, X.; Chang, L.-T.; He, L.; Liu, P.-H.; Yang, H.-J.; Tuan, H.-Y.; Chen, L.-J.; Wang, K. L. *ACS Nano* **2012**, *6*, 5710–5717.

(11) Kral, S.; Zeiner, C.; Stöger-Pollach, M.; Bertagnolli, E.; den Hertog, M. I.; Lopez-Haro, M.; Robin, E.; El Hajraoui, K.; Lugstein, A. *Nano Lett.* **2015**, *15*, 4783–4787.

(12) Lin, Y.-C.; Lu, K.-C.; Wu, W.-W.; Bai, J.; Chen, L. J.; Tu, K. N.; Huang, Y. *Nano Lett.* **2008**, *8*, 913–918.

(13) Zeiner, C.; Lugstein, A.; Burchhart, T.; Pongratz, P.; Connell, J. G.; Lauhon, L. J.; Bertagnolli, E. *Nano Lett.* **2011**, *11*, 3108–3112.

(14) Picozzi, S.; Continenza, A.; Freeman, A. J. *Phys. Rev. B: Condens. Matter Mater. Phys.* **2004**, *70*, 235205.

(15) Gaudet, S.; Detavernier, C.; Kellock, A. J.; Desjardins, P.; Lavoie, C. J. *Vac. Sci. Technol., A* **2006**, *24*, 474–485.

(16) Chao, Y.; Xu, Y.; Scholz, R.; Woo, J. C. S. *IEEE Electron Device Lett.* **2006**, *27*, 549–551.

(17) Tang, W.; Dayeh, S. A.; Picraux, S. T.; Huang, J. Y.; Tu, K.-N. *Nano Lett.* **2012**, *12*, 3979–3985.

(18) Tang, W.; Picraux, S. T.; Huang, J. Y.; Gusak, A. M.; Tu, K.-N.; Dayeh, S. A. *Nano Lett.* **2013**, *13*, 2748–2753.

(19) Mongillo, M.; Spathis, P.; Katsaros, G.; Gentile, P.; Sanquer, M.; De Franceschi, S. *ACS Nano* **2011**, *5*, 7117–7123.

(20) <http://denssolutions.com/products/nano-chip/>.

(21) den Hertog, M. I.; González-Posada, F.; Songmuang, R.; Rouviere, J. L.; Fournier, T.; Fernandez, B.; Monroy, E. *Nano Lett.* **2012**, *12*, 5691–5696.

(22) Deal, B. E.; Grove, A. S. *J. Appl. Phys.* **1965**, *36*, 3770–3778.

(23) Nemouchi, F.; Manginck, D.; Bergman, C.; Gas, P.; Smith, U. *Appl. Phys. Lett.* **2005**, *86*, 041903.

(24) Rueda-Fonseca, P.; Robin, E.; Bellet-Amalric, E.; Lopez-Haro, M.; Hertog, M. D.; Genuist, Y.; André, R.; Artioli, A.; Tatarenko, S.; Ferrand, D.; Cibert, J. *Nano Lett.* **2016**, *16*, 1637–1642.

(25) Watanabe, M.; Williams, D. B. *J. Microsc.* **2006**, *221*, 89–109.

(26) El Hajraoui, K. In situ transmission electron microscopy studies of metal-Ge nanowire solid-state reactions. Ph.D. Thesis, Université Grenoble Alpes, 2017.

(27) Tang, W.; Nguyen, B.-M.; Chen, R.; Dayeh, S. A. *Semicond. Sci. Technol.* **2014**, *29*, No. 054004.

(28) Katsman, A.; Yaish, Y.; Rabkin, E.; Beregovsky, M. J. *Electron. Mater.* **2010**, *39*, 365–370.

(29) Ogata, K.; Sutter, E.; Zhu, X.; Hofmann, S. *Nanotechnology* **2011**, *22*, 365305.

(30) Chen, Y.; Lin, Y.-C.; Huang, C.-W.; Wang, C.-W.; Chen, L.-J.; Wu, W.-W.; Huang, Y. *Nano Lett.* **2012**, *12*, 3115–3120.

(31) Yaish, Y. E.; Katsman, A.; Cohen, G. M.; Beregovsky, M. J. *Appl. Phys.* **2011**, *109*, No. 094303.

(32) El hajraoui, K.; Luong, M. A.; Robin, E.; Brunbauer, F.; Zeiner, C.; Lugstein, A.; Gentile, P.; Rouvière, J.-L.; Den Hertog, M. *Nano Lett.* **2019**, *19*, 2897–2904.

(33) Bracht, H. *Mater. Sci. Semicond. Process.* **2004**, *7*, 113–124.

(34) Becht, J. G. M.; van Loo, F. J. J.; Metselaar, R. *React. Solids* **1988**, *6*, 61–73.

(35) Werner, M.; Mehrer, H.; Hochheimer, H. D. *Phys. Rev. B: Condens. Matter Mater. Phys.* **1985**, *32*, 3930–3937.

(36) Kuper, A.; Letaw, H.; Slifkin, L.; Sonder, E.; Tomizuka, C. T. *Phys. Rev.* **1954**, *96*, 1224–1225.